Redundancy Resolution of the Human Arm and an Upper Limb Exoskeleton

Hyunchul Kim*, Levi Makaio Miller, Nancy Byl, Gary M. Abrams, and Jacob Rosen

***Abstract*—The human arm has 7 degrees of freedom (DOF) while only 6 DOF are required to position the wrist and orient the palm. Thus, the inverse kinematics of an human arm has a nonunique solution. Resolving this redundancy becomes critical as the human interacts with a wearable robot and the inverse kinematics solution of these two coupled systems must be identical to guarantee an seamless integration. The redundancy of the arm can be formulated by defining the swivel angle, the rotation angle of the plane defined by the upper and lower arm around a virtual axis that connects the shoulder and wrist joints. Analyzing reaching tasks recorded with a motion capture system indicates that the swivel angle is selected such that when the elbow joint is flexed, the palm points to the head. Based on these experimental results, a new criterion is formed to resolve the human arm redundancy. This criterion was implemented into the control algorithm of an upper limb 7-DOF wearable robot. Experimental results indicate that by using the proposed redundancy resolution criterion, the error between the predicted and the actual swivel angle adopted by the motor control system is less then 5°.**

***Index Terms*—Exoskeleton, inverse kinematic, redundancy, swivel angle.**

I. Introduction

Wearable robotic systems may improve the rehabilitation treatment as well as the quality of life of patients suffering from a wide spectrum of neuromuscular disorders such as stroke, spinal cord injury, and muscular dystrophy [1], [2]. The physical coupling between a wearable robot and the human body imposes many challenges for creating stable and natural integration between two systems. For example, their control systems must coexist, maintaining identical movements.

Manuscript recieved November 30, 2011; revised February 17, 2012; accepted March 21, 2012. Date of publication April 11, 2012; date of current version May 18, 2012. *Asterisk indicates corresponding author*.

*H. Kim was with the Department of Electrical Engineering, University of California Santa Cruz, Santa Cruz, CA 95064 USA. He is now with Atromax, Inc., Santa Clara, CA, and also with the Optodynamics, Inc., Seongnam 463-870, Korea (e-mail: hyunchul78@gmail.com).

L. Makaio Miller is with the Department of Mechanical Engineering, University of Washington, Seattle WA 98195 USA, and also with the Carbon Design Group, Seattle, WA 98105 USA (e-mail: makaio@uw.edu).

Nancy Byl is with the School of Medicine, Department of Physical Therapy and Rehabilitation Science, University of California San Francisco, San Francisco, CA 94158 USA (e-mail: BylN@ptrehab.ucsf.edu).

G. M. Abrams is with the Department of Neurology, University of California San Francisco, San Francisco, CA 94143 USA, and also with the San Francisco VA Medical Center, San Francisco, CA 94121 USA (e-mail: Gary.Abrams@ucsf.edu).

J. Rosen is with the Department of Computer Engineering and Bionics Laboratory, University of California Santa Cruz, Santa Cruz, CA 95064 USA. (e-mail: rosen@ucsc.edu).

Digital Object Identifier 10.1109/TBME.2012.2194489

The human arm is one among the many redundant subsystems of the body. With its shoulder, elbow, and wrist joints (excluding scapular motion), it has 7 degrees of freedom (DOF). However, positioning of the wrist in space and orientating the palm is a task that requires only 6 DOF [3]. As such, the human arm includes one additional DOF than is needed to complete the task. Given the redundant nature of the arm, multiple arm configurations are possible to complete a task, which is expressed mathematically by nonunique solution for the inverse kinematics [4], [5]. Despite this mathematical difficulty, the motor control provides an unique solution for the arm redundancy as the arm is moved in space. Resolving the human arm redundancy is critical to safe and effective interactions between humans and wearable robotic systems [6]. In fact, the inverse kinematics solution resolving the redundancy of these two coupled systems must be identical in order to guarantee seamless integration [1], [7].

Several criteria were previously developed aiming to resolve the human arm redundancy such as posture-based control [8], biomimetic approach [5], [9], minimum mechanical work [10], [11], minimum torque change [12], [13], kinematics, and dynamics along with task complexity [14]. The fact that the scopes of previously proposed criteria are limited in resolving the human arm redundancy may suggest that (1) additional criteria that have not yet been fully explored or defined may be used by the human motor control system and (2) multiple criteria may be simultaneously used by the motor control system, and the shift between one cluster of criteria to another cluster may be task dependent. In addition, criteria for redundancy resolution may be subject to two main deficiencies: 1) high level of computational power required for real-time implementation into a control system of a wearable robot and 2) numerical instability due to the nature of ill-posed inverse problems. The reported research proposes a new redundancy resolution criterion that was developed based on human arm kinematics data collected during daily activities that distinguish it from our previous work [7]. Furthermore, the proposed new criterion that is numerically stable and computationally efficient was implemented into the control system of a 7 DOF exoskeleton system (UL-EXO7) and its performance was experimentally tested.

II. Methods

A. Human Arm Model

The kinematics and dynamics of the human arm during activities of daily living were previously studied [3] to determine in part the specifications for the exoskeleton design [see Fig. 2(a)] [1]. The human arm is modeled as rigid links connected by three joints: shoulder joint, elbow joint, and wrist

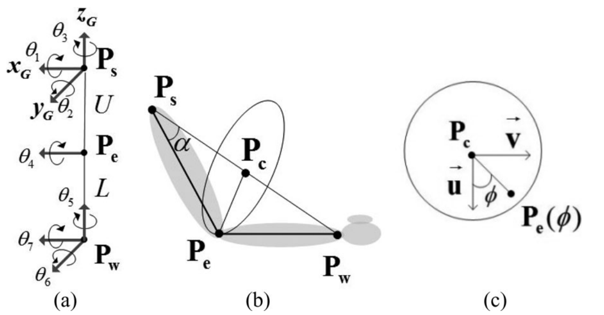

Fig. 1. Kinematic model of the human arm. (a) Global reference frame F_G defined on P_s and seven joint angles in an initial position of the right arm. (b) Extra DOF defined by a rotation axis $(P_w - P_s)$. (c) Coordinate frame at the center of the elbow circle and the swivel angle that allows the parametrizations of the elbow position by a single variable

joint [see Fig. 1(a)] while neglecting the scapular and clavicle motions [15]. The three anatomical joints include 7 DOF (shoulder joint 3 DOF, elbow joint 1 DOF, and wrist joint 3 DOF) creating a redundant 7-DOF model of the entire arm. Fig. 1(a) depicts the frame structure and rotation axis of each joint for the 7-DOF arm model.

B. Redundant Degree of Freedom—Swivel Angle

For a fixed position of the shoulder in space along with a given position and orientation of the wrist, the human arm configuration is fully defined if and only if the position of the elbow joint is fully specified. With its three joints the arm forms a triangle with one corner at the shoulder joint P_s, one corner at the elbow joint P_e, and the last corner at the wrist joint P_w [see Fig. 1(b)]. Both the shoulder and wrist joints are spherical joints allowing the rotation of point P_e around the vector $(P_w - P_s)$ [see Fig. 1(b)]. A local coordinate system allocated at the center of the elbow circle P_c with three orthogonal unit vectors ($\vec{n}$, $\vec{u}$, $\vec{v}$) provides a reference coordinate system to define and measure the swivel angle ϕ of the elbow [see Fig. 1(c)]

$$\vec{n} = \frac{(P_w - P_s)}{\|P_w - P_s\|}, \vec{u} = \frac{(\vec{a} - (\vec{a}\cdot\vec{n})\vec{n})}{\|\vec{a} - (\vec{a}\cdot\vec{n})\vec{n}\|}, \vec{v} = \vec{n} \times \vec{u}. \quad (1)$$

Setting $\vec{u} = -\vec{z}$ in (1), position the elbow at its lowest point when $\phi = 0$ [16]. Given the geometry depicted in Fig. 1, the position of the elbow can be expressed as a function of ϕ [17] such that

$$P_c = P_s + U\cos(\alpha)\cdot\vec{n}, P_e = R\left[\cos(\phi)\vec{u} + \sin(\phi)\vec{v}\right] + P_c \quad (2)$$

$$\cos(\alpha) = \frac{U^2 - L^2 - \|P_w - P_s\|^2}{-2L^2\|P_w - P_s\|}, R = U\sin(\alpha) \quad (3)$$

where U and L are the length of the upper and lower arm segments, respectively [see Fig. 1(a)] and ϕ is defined as the swivel angle.

C. Kinematic Model and Exoskeleton Control Algorithm

The forward kinematics defines the position of the end effector $P_0 \in R^m$ expressed in the base coordinate system of a serially articulated mechanism with n-links such as a human arm or an exoskeleton robot as a function of joint space variables $\theta = [\theta_1, \theta_2, \ldots, \theta_n] \in R^n$ as follows:

$$P_0 = g_d P_T = T_1T_2T_3T_4T_5T_6T_7 g_{st} P_T = T_1T_2T_3T_4T_5T_6T_7 P_T' \quad (4)$$

where T_i and g_{st} denote the 4×4 homogeneous transformation matrix defining the rotation and translation at the ith joint axis and the transformation between the tool and base frames at $\theta = 0$ based on the exponential coordinates system approach [18]. Unlike the Denavit–Hartenberg (DH) parameter approach representing the relative motions of each link with respect to the previous link, g_{st} translates the end effector P_T in the local tool frame to P_T' in the global base frame. Thus, T_i performs the rotations and translations at the ith joint axis in the global base frame. There is not a simple one-to-one mapping between the exponential coordinates and the DH parameters approach but both have the same form of final transformation matrix g_d in (4). In this approach, T_i for rigid body motion is defined as

$$T_i = \begin{bmatrix} R_i & P_i \\ 0 & 1 \end{bmatrix} \quad (5)$$

where R_i is the 3×3 rotation matrix about the axis $\vec{\omega}_i$ and P_i equals to $(P_{q_i} - R_i P_{q_i})$, where P_{q_i} is a point that the ith axis of rotation passes through [19].

The exoskeleton controller generates the desired joint angles for the given end-effector position $P_0 \in R^m$ by solving the inverse kinematic problem of (4). One of the solutions to the inverse kinematics problem is based on the existing mapping between the joint velocity $\dot{\theta}$ and the end-effector velocity $\dot{P}_0$ through the Jacobian matrix J that is defined as $\dot{P}_0 = J\dot{\theta}$. Given the redundant nature of the system, the Jacobian pseudoinverse J^+ is used for solving the inverse kinematic problem [20]. Then, the general solution is given by

$$\dot{\theta} = J^+\dot{P}_0 + \left(J^+J - I_n\right)Z, J^+ = J^T\left(J\cdot J^T\right)^{-1} \quad (6)$$

where J^+ is the pseudoinverse matrix of J for an underdetermined (redundant) case$(n > m)$, I_n is the $n \times n$ identity matrix, and Z is an arbitrary vector. In (6), $J^+\dot{P}_0$ is the minimum norm and homogeneous solution of $\dot{P}_0 = J\dot{\theta}$. The term $(J^+J - I_n)$ maps $\dot{\theta}$ onto the null space of J that enables various joint configurations without affecting the end-effector position and velocity. Thus, by applying the proper cost function producing a specific Z vector as a secondary criterion, specific arm postures can be achieved while, at the same time, tracking a given end-effector trajectory as a primary goal. One effective way of defining Z vector is by using the objective function H and projecting it onto the null space of the Jacobian through $(J^+J - I_n)$. Then, (6) can be written as

$$\dot{\theta} = J^+\dot{P}_0 + \alpha_w\left(J^+J - I_n\right)\frac{\partial H(\theta, \theta_c(t))}{\partial\theta} \quad (7)$$

where α_w is a weighting parameter such that $\alpha_w > 0$. The following quadratic objective, called joint angle availability, was initially used for the robotic manipulator in order to avoid joint limits [21]

$$H(\theta, \theta_c(t)) = \sum_{i=1}^{n}\left(\frac{\theta_i - \theta_{ci}(t)}{\Delta\theta_i}\right)^2,$$
$$\theta_c(t) = [\theta_{c1}(t), \theta_{c2}(t), \ldots \theta_{cn}(t)] \quad (8)$$

where θ_i is the joint angle, $\Delta\theta_i$ is the operating range of the joint i, and $\theta_{ci}(t)$ is the desired joint angle of joint i. Utilizing (8) in (7) enables the joint configuration of a redundant manipulator to remain close to $\theta_{ci}(t)$. Assuming that the wrist orientation does not affect the human arm during a reaching task and the swivel angle is only affected by the wrist position, it is possible to match the the configuration of the exoskeleton with the posture of the human arm by properly estimating the desired swivel angle ϕ that in turn defines the desired joint angles of the shoulder [$\theta_{c1}(t)$, $\theta_{c2}(t)$, and $\theta_{c3}(t)$]. Note that $\theta_{c4}(t)$ can be geometrically defined while $\theta_{c5}(t)$, $\theta_{c6}(t)$, and $\theta_{c7}(t)$ defining the orientation of the wrist joint can be determined by the operator or set as an initial value.

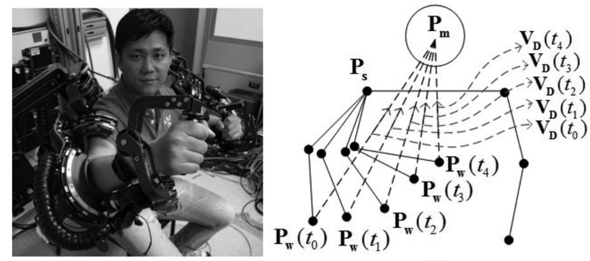

(a) (b)

Fig. 2. (a) Human wearing 7-DOF upper limb exoskeleton that supports 95% of the workspace of the human arm. (b) Graphical representation of the proposed redundancy resolution criterion indicating that for the given wrist position $P_W(t_i)$ at any given time t_i, there is a virtual path $V_D(t_i)$ toward the subject's head.

III. Swivel Angle Estimation

The human arm provided inspiration for the design of many industrial robotic arms in terms of joint configurations, link lengths, and the ratio between them. Unlike industrial robotic systems that can be freely positioned and oriented with respect to their external environment, analyzing the human arm must be done in the context of the human body anatomy and in particular the head. Among the many functions that the human arm is capable of, one of its primary functions is to facilitate feeding, and therefore, the head is one of its primary targets. Moreover, given the role of the head as a cluster of sensing organs and the importance of the arm manipulation to deliver food to the mouth to sustain life, we hypothesized that *For the natural reaching and grasping tasks, the value of swivel angel selected by human motor control system to resolve the arm redundancy is selected to efficiently retract the palm to the head.*

This implies that during the arm movement toward an actual target, the virtual target point on the head is also set to efficiently retract the palm to the virtual target on the head at any time. The virtual destination on the head is defined as P_m and the trajectory $V_D(t_i)$ to P_m is set up while the hand moves within workspace of the arm as part of its reaching task [see Fig. 2(b)]. Note that the scope of the research is limited to the swivel angle estimation for the unconstrained and natural reaching/grabbing activity of the human arm. Here, the unconstrained reaching/grabbing task means that there are no obstacles between the human and the target.

This hypothesis is supported by the intracortical stimulation experiments to evoke coordinated forelimb movements in the awake primate [22], [23], [24]. It has been reported that each stimulation site produced a stereotyped posture in which the arm moved to the same final position regardless of its posture at the initial stimulation. In a more recent study, Stepniewska *et al.* [24] systematically mapped the parietal lobe of prosimians using electrical stimulation and found distinct functional zones in which different types of movement were evoked. These movements included eye movements, reaching, bringing the hand to the mouth, aggressive displays, and defensive movements [22], [24]. In the most complex example [23], the monkey formed a frozen pose with the hand in a grasping position in front of the open mouth. The reported experimental result implies that during the arm movement toward an actual target, the virtual target point on the head can be set for the potential retraction of the palm to the virtual target [see Fig. 2(b)].

A. Manipulability Ellipsoid and Redundancy Resolution Criteria

The principle concept that is stated as part of the hypothesis is associated with the manipulability ellipsoid. For the combined arm joint velocities satisfying the condition stated as $\Sigma_{i=1}^{n}\dot{\theta}_i^{\,2} = 1$, the hand velocity as a function of the arm joint velocity is described by an ellipsoid known as the manipulability ellipsoid. The orientation of the ellipsoid with its three major axes is defined by the eigenvectors of the Jacobian and the lengths of the major axes are defined by the eigenvalues of the Jacobian [25]. The largest among the major axes of the manipulability ellipsoid defines the direction in which the hand is more likely to move and the best mapping between the arm joint space and the end-effector (hand) Cartesian space [see Fig. 3(b)] [26]. Point P_m is defined as the attraction point for the head and point P_w defines the location of the wrist joint position. A straight virtual trajectory is then defined passing through points P_m and P_w [see Fig. 2(b)]. Then, the proposed criterion for the arm redundancy resolution is such that *the selected swivel angle for the natural arm posture is chosen in a way that the projection of the longest axis of the manipulability ellipsoid onto the virtual trajectory* $(P_m - P_w)$ *is maximized.* By doing this, the proposed hypothesis in the previous section can be mathematically formulated as follows.

1) Manipulability Ellipsoid on the Wrist: Let the plane S be defined by three point P_w, P_e, and P_s. The longest axis of the manipulability ellipsoid is aligned along plane S and its magnitude σ_1 is defined as

$$\sigma_1 = \sqrt{\frac{\left(\left(L_{ws}^2 + L_{we}^2\right) + \left(L_{ws}^2 + L_{we}^2\right)c_1\right)}{2}}$$
$$c_1 = \sqrt{1 - c_2}, c_2 = 4L_{we}^2 L_{ws}^2 \sin(\varphi)^2 / \left(L_{ws}^2 + L_{we}^2\right)^2$$

where $L_{ws} = \|P_w - P_s\|$ and $L_{we} = \|P_w - P_e\|$. This result is based on the following derivation and only the right-hand side is considered for analysis.

Proof: A new coordinate frame is defined with an origin at P_s [see Fig. 3(a)] for the computational purpose. In this frame, the *z*-axis is orthogonal to the plane S and the *x*-axis is aligned

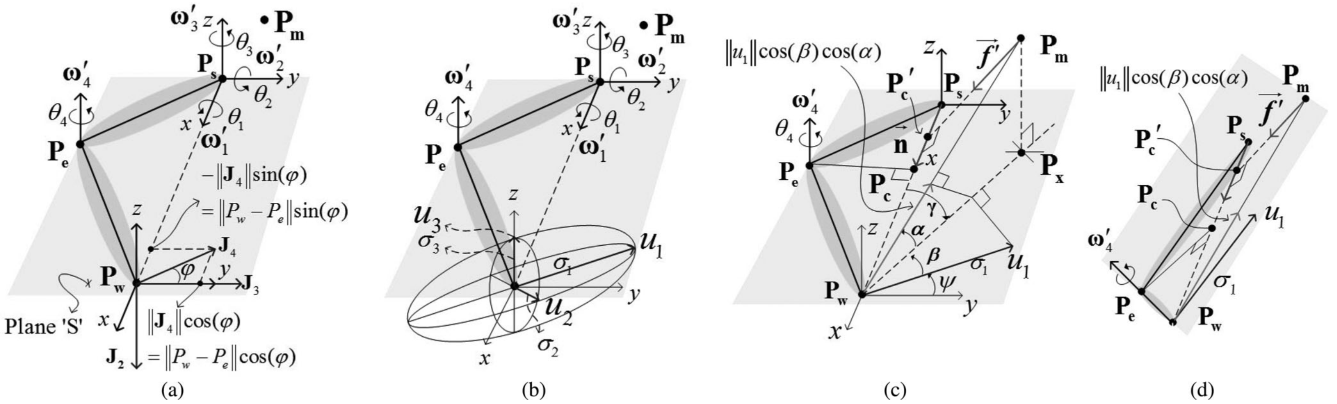

Fig. 3. New coordinate system composed of P_w, P_e, P_s, and P_m. (a) Each element J_i in the Jacobian matrix is defined with respect to the newly defined frame on the shoulder where the x axis is defined as $(P_w - P_s)/\|P_w - P_s\|$ and y-axis sits on the plane S composed of P_w, P_e and P_s. The new frame on the shoulder is defined for the convenience of the calculation. (b) Manipulability ellipsoid on the wrist position. u_1,u_2, and u_3 indicate the three major axes of the ellipsoid with magnitude of σ_1,σ_2, and σ_3. (c) Highest manipulability direction vector u_1 projected on the $(P_m - P_w)/\|P_m - P_w\|$ is marked as an arrow along $(P_m - P_w)$ and its magnitude can be represented as $\|u_1\|\cos(\alpha)\cos(\beta)$. (d) It shows the specific elbow position for the given wrist position that maximizes the manipulability projected on the virtual trajectory. In this configuration P_m,P_s,P_e, and P_w are on the same plane.

with the vector $(P_w - P_s)$. Then, the relationship between the end-effector velocity $\dot{\mathbf{P}} = [\dot{x_w}\,\dot{y_w}\,\dot{z_w}]^T$ and the joint velocity $\dot{\theta}_{1234} = [\dot{\theta}_1\dot{\theta}_2\dot{\theta}_3\dot{\theta}_4]^T$ is defined as follows:

$$\dot{\mathbf{P}} = \mathbf{J}\dot{\theta}_{1234} = [\mathbf{J}_1\mathbf{J}_2\mathbf{J}_3\mathbf{J}_4]\dot{\theta}_{1234},$$
$$\mathbf{J}_i = \begin{cases} \omega_i' \times (P_w - P_s), i = 1, 2, 3 \\ \omega_i' \times (P_w - P_e), i = 4 \end{cases} \tag{9}$$

where ω_i' denotes the rotation axis of the ith joint. By introducing a new variable φ [see Fig. 3(a)] to represent $\mathbf{J}_4$ and using the fact that $\omega_1' = \vec{x}$, $\omega_2' = \vec{y}$ and $\omega_3' = \vec{z}$ in Fig. 3(a), we have

$$\dot{\mathbf{P}} = \begin{pmatrix} 0 & 0 & -L_{we}\sin(\varphi) \\ 0 & L_{ws} & L_{we}\cos(\varphi) \\ -L_{ws} & 0 & 0 \end{pmatrix} \dot{\theta}_{234} = \mathbf{J}_{234}\dot{\theta}_{234} \tag{10}$$

where the full derivation for (10) can be found in [7]. According to the singular value decomposition, $\mathbf{J}_{234}$ can be represented as $\mathbf{J}_{234} = \mathbf{UDV}^T$ where $\mathbf{U} = [u_1 u_2 u_3]$, $\mathbf{V} = [v_1 v_2 v_3]$ and $\mathbf{D} = \mathrm{diag}[\sigma_1\sigma_2\sigma_3]$. The u_i in the left singular vector $\mathbf{U}$ indicates one of the three axis constructing the manipulability ellipsoid and singular value σ_i in $\mathbf{D}$ indicates the magnitude of the u_i as shown in Fig. 3(b). Note that u_i and σ_i are the eigenvectors and square root of the nonzero eigenvalues of $\mathbf{J}_{234} \cdot \mathbf{J}_{234}^*$. Solving $\det(\mathbf{J}_{234} \cdot \mathbf{J}_{234}^* - \lambda\mathbf{I}) = 0$ allows to obtain u_i and $\sigma_i (= \sqrt{\lambda_i})$. Based on Sarrus's rule [25], the following expressions for the eigenvalues are obtained

$$\lambda_{1,2} = \frac{\left(L_{ws}^2 + L_{we}^2\right) \pm \left(L_{ws}^2 + L_{we}^2\right) c_1}{2}, \lambda_3 = L_{ws}^2$$
$$(\lambda_1 > \lambda_2), c_1 = \sqrt{1 - c_2},$$
$$c_2 = 4L_{we}^2 L_{ws}^2 \sin(\varphi)^2 / \left(L_{ws}^2 + L_{we}^2\right)^2.$$

One may note that $0 \leq c_2 \leq 1$ and $0 \leq c_1 \leq 1$ such that $\lambda_{1,2}$ are not complex numbers. The relationships between λ_1, λ_2, and λ_3, is studied by using two individual cases

$\mathbf{case1}: (L_{ws} \geq L_{we})$

$$\begin{aligned} \lambda_1 - \lambda_3 &= \frac{\left(L_{ws}^2 + L_{we}^2\right) + \left(L_{ws}^2 + L_{we}^2\right) c_1}{2} - L_{ws}^2 \\ &\geq \frac{\left(L_{we}^2 - L_{ws}^2\right) + \left(L_{ws}^2 + L_{we}^2\right) c_{\min 1}}{2} \\ &= \frac{\left(L_{we}^2 - L_{ws}^2\right) + \left(L_{ws}^2 + L_{we}^2\right)\sqrt{1 - c_{\max 2}}}{2} \\ &= \frac{\left(L_{we}^2 - L_{ws}^2\right) + \sqrt{\left(L_{ws}^2 - L_{we}^2\right)^2}}{2} = 0 \end{aligned} \tag{11}$$

where $c_{\min 1}$ and $c_{\max 2}$ are the minimum and maximum value of c_1 and c_2, respectively. The term $c_{\max 2}$ in (11) is defined as

$$\begin{aligned} c_{\max 2} &= \max(4L_{we}^2 L_{ws}^2 \sin(\varphi)^2)/\left(L_{ws}^2 + L_{we}^2\right)^2 \\ &= 4L_{we}^2 L_{ws}^2/\left(L_{ws}^2 + L_{we}^2\right)^2 \end{aligned}$$

$\mathbf{case2}: (L_{ws} < L_{we})$

$$\begin{aligned} \lambda_1 - \lambda_3 &= \frac{\left(L_{ws}^2 + L_{we}^2\right) + \left(L_{ws}^2 + L_{we}^2\right) c_1}{2} - L_{ws}^2 \\ &\geq \frac{(1 + c_{\min 1})\left(L_{ws}^2 + L_{we}^2\right)}{2} - L_{ws}^2 \\ &= \frac{\left(L_{we}^2 - L_{ws}^2\right)}{2} \geq 0 \end{aligned} \tag{12}$$

where the first inequality in (12) is based on the fact that $c_{\min 1} = \min[c_1] = 0$. The second inequality in (12) is valid since $L_{ws} < L_{we}$. Therefore, we conclude that $\lambda_1 \geq \lambda_3$ for all possible values of L_{ws}. It implies that the magnitude of the longest axis in the manipulability ellipsoid is

$$\sigma_1 = \sqrt{\lambda_1} = \sqrt{((L_{ws}^2 + L_{we}^2) + (L_{ws}^2 + L_{we}^2)\, c_1)/2}. \tag{13}$$

Based on the fact that the direction of the major axis of the manipulability ellipsoid corresponds to the eigenvector of the following (14), the eigenvector u_1 is obtained by applying the corresponding eigenvalue λ_1 to λ in the following equation:

$$(\mathbf{J}_{234} \cdot \mathbf{J}^*_{234})\,\mathbf{X} = \lambda \mathbf{X}, \mathbf{X} = [x\ y\ z]^T. \tag{14}$$

Then, the direction of the eigenvector $\mathbf{X}$ in (14) is defined as

$$\begin{aligned} y &= \frac{\lambda_1 + L^2_{we}\sin(\varphi)\cos(\varphi)}{-L^2_{we}\sin(\varphi)^2} x \\ &= \left(-\frac{\lambda_1}{L^2_{we}\sin(\varphi)^2} - \frac{1}{\tan(\varphi)}\right) x, z = 0. \end{aligned} \tag{15}$$

Considering the joint limit of the exoskeleton robot [6], it is assumed that $0 < \varphi \leq \pi/2$. Note that when $\varphi = 0$, the arm is in a singular position. Then, based on the fact that $\lambda_1 > 0$, the slope in (15) becomes negative. Fig. 3(c) depicts the direction of u_1 on plane S.

2) Optimum Swivel Angle: Given the constraint $\sum_1^n \dot{\theta}_i^2 = 1$, the longest axis of the manipulability ellipsoid defines the best mapping between joint and task space, and the direction along which the hand is more likely to move than any other direction. The optimum swivel angle is, therefore, defined such that the projection of the longest axis u_1 on the vector $(P_m - P_w)$ is maximized for the given wrist position as in (16). Note that $(P_m - P_w)$ is the shortest path between the wrist and the attraction point at the head

$$\begin{aligned} \phi &= \arg \max_{\alpha,\beta \in [0\ \frac{\pi}{2}]} u_1^T\,(P_m - P_w) \\ &= \arg \max_{\alpha,\beta \in [0\ \frac{\pi}{2}]} \|u_1\|\|P_m - P_w\|\cos(\alpha)\cos(\beta) \end{aligned} \tag{16}$$

where α and β indicate the angle between $(P_m - P_w)$ and plane S, and the angle between u_1 and the projection of $(P_m - P_w)$ onto S equivalently $(P_x - P_w)$ [see Fig. 3(c)]. Note that the projected portion of u_1 onto $(P_m - P_w)/\|P_m - P_w\|$ is represented as $\|u_1\|\cos(\alpha)\cos(\beta)$ marked as a vector pointing at P_m on $(P_m - P_w)$ in Fig. 3(c). By introducing γ which is the angle between $(P_s - P_w)$ and $(P_x - P_w)$ from Fig. 3(c), we know

$$\cos(\beta) = \cos(\pi/2 - \gamma - \psi) = \sin(\gamma + \psi) \tag{17}$$

$$\begin{aligned} &= c_3\sin(\gamma) + c_4\cos(\gamma) \\ &= \frac{c_3\|P_x - P_c'\| + c_4\|P_c' - P_w\|}{\|P_x - P_w\|} \end{aligned} \tag{18}$$

$$= \frac{c_3\|\vec{f}' \cdot \frac{P_c - P_e}{\|(P_c - P_e)\|}\| + c_4\|P_c' - P_w\|}{\|P_x - P_w\|} \tag{19}$$

$$= \frac{c_3\|\vec{f}'\|\cos(\eta) + c_4\|P_c' - P_w\|}{\|P_x - P_w\|} \tag{20}$$

where c_3 and c_4 are $\cos(\psi)$ and $\sin(\psi)$, respectively. Note that (17) is based on the fact that $(\gamma + \psi) \leq \pi/2$ and P_c' in (18) is the projection of $(P_m - P_w)$ onto $\vec{n}$ as shown in Fig. 3(c), η in (20) is the angle between $\vec{f}'$, which is $\vec{f} - (\vec{f} \cdot \vec{n})\vec{n}$ in Fig. 3(c), and $(P_c - P_e)$. Based on the fact that $\cos(\alpha) = \|P_x - P_w\|/\|P_m - P_w\|$, results in

$$\begin{aligned} \cos(\alpha)\cos(\beta) &= \frac{c_3\|\vec{f}'\|\cos(\eta) + c_4\|P_c' - P_w\|}{\|P_m - P_w\|} \\ &= c_5\cos(\eta) + c_6 \end{aligned}$$

where constants c_5 and c_6 are $c_3\|\vec{f}'\|/\|P_m - P_w\|$ and $c_4\|P_c' - P_w\|/\|P_m - P_w\|$. Plugging (21) into (16), results in

$$\phi = \arg \max_{\alpha,\beta \in [0\pi/2]} = [\|u_1\|\|P_m - P_w\|\,(c_3\cos(\eta) + c_4)]. \tag{21}$$

When $\eta = 0$, (21) is maximized and consequently α in (21) becomes zero. Under this condition, plane S is coplanar with the plane defined by P_m, P_s, and P_w as shown in Fig. 3(d). Therefore, the swivel angle satisfying (21) for a given P_m, P_w, and P_s is computed as follows:

$$\begin{aligned} \vec{f} = P_w - P_m, \vec{f}' &= \vec{f} - \left(\vec{f} \cdot \vec{n}\right)\vec{n}, \phi \\ &= \arctan 2\left(\vec{n} \cdot \left(\vec{f}' \times \vec{u}\right), \vec{f}' \cdot \vec{u}\right). \end{aligned} \tag{22}$$

Once the swivel angle estimation is completed, the actual joint angles $\{\theta_1, \theta_2, \theta_3, \theta_4\}$ can be computed by solving the following equations [19]:

$$T_1T_2\begin{bmatrix} P_{e_o} \\ 1 \end{bmatrix} = \begin{bmatrix} P_e(\phi) \\ 1 \end{bmatrix}, T_1T_2T_3T_4\begin{bmatrix} P_{w_0} \\ 1 \end{bmatrix} = \begin{bmatrix} P_w \\ 1 \end{bmatrix} \tag{23}$$

where $P_e(\phi)$ is the elbow position computed by combining (3) and (22). Note that P_{w_0} and P_{e_0} in (23) represent the initial position of the wrist and the elbow based on the exponential coordinates approach. The complete derivation to solve (23) also can be found in [19]. Then, by substituting the computed joint angles with $\theta_c\,(t)$ in (8), desired joint angles to control exoskeleton robot are defined based on (7). Based on (22), it can be shown that a singularity occurs when $\vec{f}'$ and $\vec{u}$ are aligned.

IV. Experimental Methodology

A. Subject Definition

Ten right-handed healthy subjects(eight were males and two were females) participated in the experiment. The average age was 32 years. Based on the collected kinematic data, the swivel angles (ϕ_{act}) were directly measured and compared with corresponding values estimated by the proposed algorithm in (22).

B. Experimental Tasks

Three types of experimental protocols were derived from activities of daily living which included 1) arm reaching and pointing, 2) object manipulations both from a reference point to predefined locations in space in an unconstrained environment as well as 3) arm reaching and grasping while following a constrained trajectory. Fig. 4(c), (d), and Table II define the the three experimental setups.

1) Body Postures: Each subject was tested in a sitting posture with his/her torso restrained from torsional movements. The distance between the subject and the table was adjusted based on the length of the subject's arm in order to a avoid a full stretch of

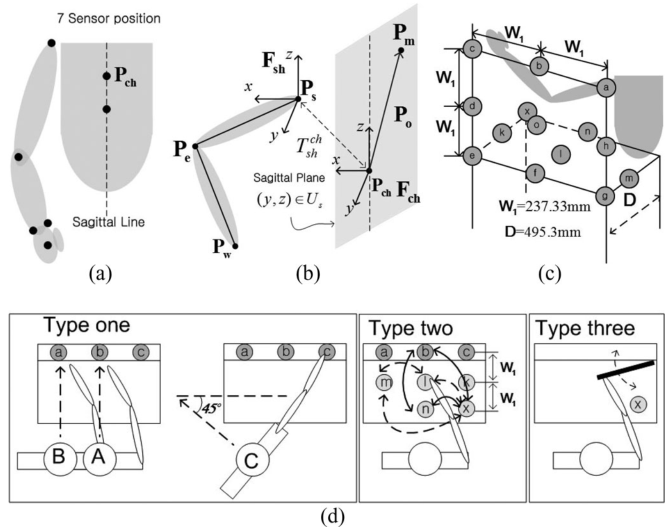

Fig. 4. (a) Positions of LED markers: Shoulder(Arcomioclavicular joint), Elbow(Lateral edge of the Ulna), Wrist(Medial and Lateral edge of the distal end of the radius and ulna), Palm(between 2 and 3 metacarples) and Torso(Upper and lower sternum). (b) $P_{\rm ch}$ is the origin of the frame $F_{\rm ch}$ and P_o is the offset between $P_{\rm ch}$ and P_m. Homogeneous transform matrix $T_{\rm sh}^{\rm ch}$ is defined between frame $F_{\rm sh}$ and $F_{\rm ch}$. (c) Target locations and dimensions: height of the table-top from the ground = 736.6 mm. (d) Three types of reaching tasks. In condition "A" and "B" of type one, torso is facing "b" and "a" of the task space, respectively, while the condition "C" is with the torso turned 45° counterclockwise off the Sagittal alignment and abducted hand points "c."

the arm (singular configuration). For the type one protocol in the left box of Fig. 4(d), each subject was positioned with respect to the table in three different body postures. In body posture A, the subject faced the table and his/her body was position such that the table and the subject's body center lines were aligned. In body posture B, the subject faced the table as previously but center line was shifted to the left such that it was aligned with the edge of the table. In body posture C, the body of the subject alignment was the same as in (B) but the torso was rotated by 45° counterclockwise. For the remaining two protocols, the body is in posture A.

2) Targets and Objects: In the type one protocol, the subject used his/her index finger to point to the designated targets. In the type two protocol the subjects grasped a ping-pong (PP) ball and a water bottle (WB) with the orientation of the wrist determined by themselves. The two objects were selected to see the effect of the wrist orientation on the swivel angle during object manipulations. Given the ping-pong ball geometry it has a negligible effect on the wrist orientation as opposed to the water bottle that dictates a specific final orientation and, therefore, affects the wrist orientation. The subjects repeat the experiments for the two different directions (LR: Left and Right) and (BF:Back and Forth) that resulted in four different tasks (LR:PP, LR:WB, BF:PP, and BF:WB). In the type three protocol, the subject grasped a cabinet door handle. This protocol strictly determines the wrist orientation.

3) Sequence: Each subject was instructed to position the hand in an initial location ("o" or "x") and then move the hand in a self-paced fashion between predefined locations as defined in Fig. 4(d). The sequences are defined in Table II.

C. Data Collection

The kinematic data of the human arm are collected using the Phasespace motion capture system (Phasespace, Inc.) including eight cameras with submillimeter accuracy. Active LED makers were attached to a subject's body at key anatomical locations including shoulder(P_s), elbow(P_e), wrist(P_w), and chest($P_{\rm ch}$) [see Fig. 4(a)]. The markers' locations were sampled at 240 Hz.

D. Data Post Processing: Optimum P_m Estimation

Given the anthropometric differences between the subjects, the optimal target location P_m for each subject was calculated. The human body is considered to be symmetric and torsional movement of the torso is ignored. The LED markers $P_{\rm ch}$ on the chest (see Fig. 3) as well as P_m are, therefore, located on the Sagittal plane [see Fig. 4(b)]. A reference frame $F_{\rm ch}$ is attached to $P_{\rm ch}$. As a result, the location of P_m is represented by a fixed vector (time invariant) P_o expressed in frame $F_{\rm ch}$ (the Sagittal plane) as follows:

$$\begin{bmatrix} P_m(t) \\ 1 \end{bmatrix} = \begin{bmatrix} P_{\rm ch}(t) \\ 1 \end{bmatrix} + T_{\rm sh}^{\rm ch}(t) \begin{bmatrix} P_o \\ 1 \end{bmatrix} \tag{24}$$

where P_o is a vector representing a constant time-invariant translation offset from $P_{\rm ch}$ expressed in frame on $P_{\rm ch}$ and $T_{\rm sh}^{\rm ch}$ is the homogeneous transform matrix between the frame attached to the shoulder and the frame attached to the chest as depicted in Fig. 4(b). Then, according to (22), the optimum offset P_o is chosen to minimize the difference between $\phi(t)_{\rm est}$, estimated swivel angle based on (22) and $\phi(t)_{\rm act}$, calculated swivel angle given the measured joint angels

$$\arg \min_{y,z \in U_s} \int_y \int_z \left(\int_{t_x}^{t_x+T} |\phi(t)_{\rm act} - \phi(t, P_o(y,z))_{\rm est}| dt \right) dz dy \tag{25}$$

where U_s represent (y, z) coordinate pairs on the Sagittal plane [see Fig. 4(b)]. Since it is assumed that P_m is located on the Sagittal plane, $x_{\rm opt}$ is same as the x-coordinate of $P_{\rm ch}(t)$. Only a subset of the data were used to calculate the optimal location of P_m, as a result, T in (25) corresponds to 1/5 of total data recording time. The estimated location of (y, z) defining P_o is summarized in the last column of Table I. In addition Fig. 5 shows the realtime trajectory of P_m with respect to the right arm shoulder position. It appears that the trajectory is around the actual head region. However, note that due to the limited accuracy of the motion captures system, position of the marker on each joint and the lack of scapular movement in the human arm model, the estimated P_m for each experimental task is not identical.

V. Results

A. Swivel Angle Estimation

For the performance estimation, the mean and standard variation of the absolute difference $e(t) = |\phi(t)_{act} - \phi(t, P_o(x,z))_{\rm est}|$ between the the measured swivel angle

TABLE I
AVERAGED ABSOLUTE DIFFERENCES BETWEEN MEASURED AND ESTIMATION SWIVEL ANGLES

Subject	Protocol Type one			Potocol Type two				Protocol Type three	$P_o(y,z)$
	A	B	C	LR:PP	LR:WB	BF:PP	BF:WB	Opening cabinet	(mm)
1	2.34°±1.52	2.72°±1.85	3.77°±3.01	8.66°±4.15	4.10°±3.05	5.04°±3.02	4.96°±3.70	4.50°±3.00	(-160, 280)
2	3.22°±2.34	3.99°±2.58	2.08°±1.36	4.82°±2.24	5.79°±2.98	7.13°±3.61	6.11°±3.94	4.03°±2.92	(-140, 320)
3	5.40°±2.59	6.25°±3.00	7.13°±3.38	4.80°±2.87	3.45°±2.64	4.07°±2.79	4.93°±3.12	4.67°±2.69	(-160, 390)
4	5.12°±2.59	3.84°±2.20	3.05°±1.73	9.04°±5.51	5.16°±4.27	5.30°±2.75	6.80°±3.60	4.09°±2.92	(-70, 290)
5	8.07°±4.32	4.63°±2.84	3.42°±2.10	7.91°±3.31	8.50°±4.52	8.85°±6.18	5.73°±3.55	7.73°±5.12	(-160, 170)
6	6.08°±4.22	4.68°±3.49	4.82°±3.30	4.63°±4.14	3.93°±2.17	3.22°±2.04	4.22°±3.06	4.84°±3.74	(-150, 300)
7	4.32°±2.62	4.94°±2.07	2.98°±1.90	8.35°±5.17	7.18°±3.94	5.48°±2.72	5.88°±3.17	4.81°±3.06	(-80, 250)
8	3.82°±2.82	3.64°±2.56	3.77°±3.01	8.21°±5.55	5.29°±3.07	3.62°±2.11	5.54°±3.76	5.64°±2.97	(140, 330)
9	2.19°±1.64	4.96°±2.22	3.65°±2.42	7.15°±3.64	4.52°±2.70	6.24°±3.89	6.35°±3.62	6.20°±4.21	(-100, 310)
10	3.85°±2.74	4.69°±3.23	5.98°±3.50	9.36°±4.55	5.07°±4.12	6.50°±3.56	8.17°±4.93	2.73°±2.17	(-60, 220)

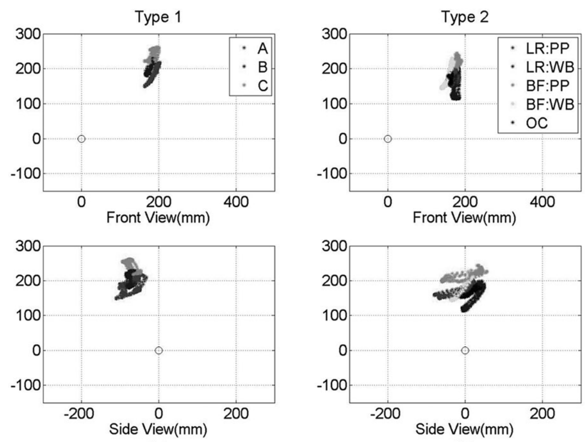

(a) (b)

Fig. 5. (a) and (b) shows exemplary plots of $P_m(t)$ for all task types from one subject. Upper and lower rows indicate the front and side views of (looking at the right shoulder) P_m with respect to the shoulder(reference frame) in millimeter scale. Black empty circles indicate the right arm shoulder position P_{sh}. P_m is individually estimated for each experiment and marked as a different color depending on the task type.

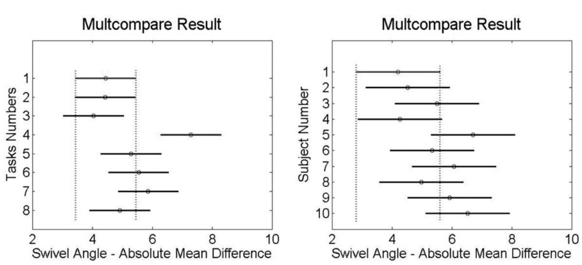

(a) (b)

Fig. 6. (a) ANOVA test with respect to types of tasks ($P<0.05$). 1, 2, and 3 in y-axis means the type one task A, B, and C. 4,5,6, and 7 in y-axis mean the type two LR:PP, LR:WB, BF:PP and BF:WB, respectively. 8 in y-axis means the type three task. (b) ANOVA test with respect to different subject ($P<0.05$)

TABLE II
SUMMARY OF EXPERIMENT PROTOCOL

Type	Body Posture	Sequence	Number of Repetitions	Object
1	A,B,C	$o \to a \to b \to c \to d \to e \to f \to g \to h$	5	None
2	A:LR A:BF	$x \to l \to m \to x \to m \to l \to x$ $x \to n \to b \to x \to b \to n \to x$	3 3	Ping pong ball/ Water bottle
3	A	$x \to Opencabinet \to Closecabinet \to x$	3	Cabinet door

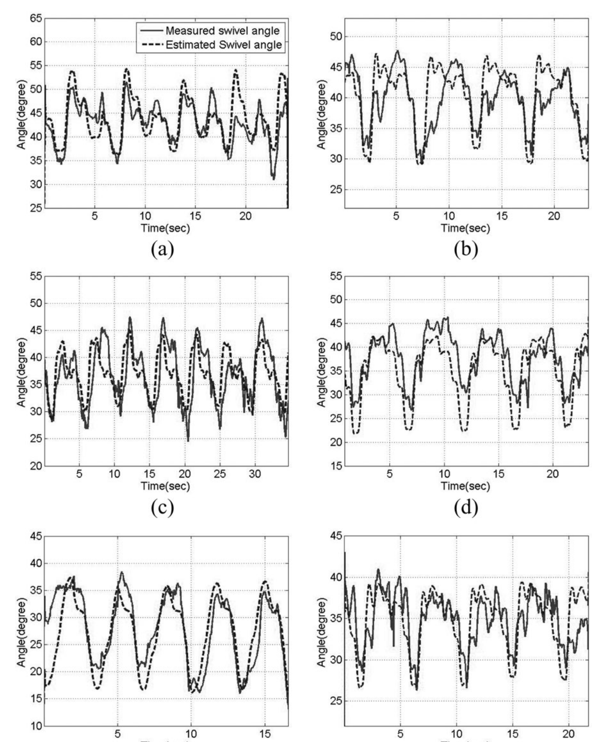

(a) (b) (c) (d) (e) (f)

Fig. 7. Comparison between estimated swivel angle(dotted line) and calculated swivel angle(solid line) for type one task. Each row shows the comparison result for type one(A), (B), and (C) from the subjects. The first and second columns are from subject 1 and 2, respectively.

collected from the subjects during the experiments and the estimated swivel angle based on the proposed criterion were calculated. The performance estimation results for all the tasks are summarized in Table I. The same difference is plotted for multiple repetitions of two subjects in Figs. 7–9. The periodic nature of these plots are due to the multiple repetitions of the same task. The swivel angle differences are in the range of 2.1°–8.1° for type one protocol, 3.5°–9.4° for type two protocol, and 2.7°–6.2° for type three protocol. Averaging the difference of the swivel angle across the entire data base indicates that the estimated value is different by less than 5° from the measured value. In Fig. 6, two ways ANOVA analysis of the data with a confidence level of 95% indicated experimental protocol type two (LR:PP) is significantly different from all the other tasks and there are no significant difference between the subjects.

There are several sources for error resulting from: 1) inherent measurement error generated by the motion capture system, 2) torso rotation that took place in spite of the physical constraints,

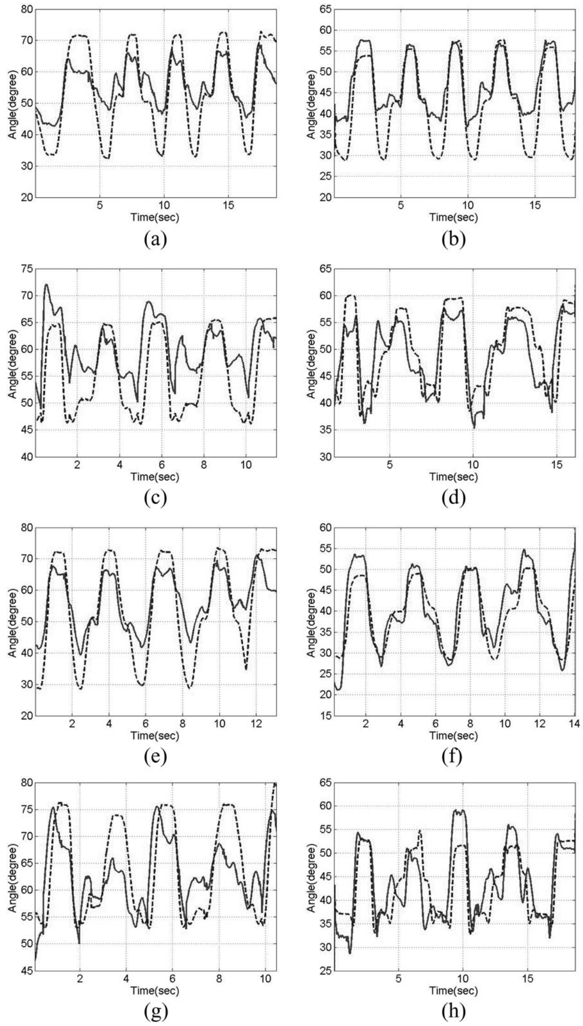

Fig. 8. Comparison between estimated swivel angle(dotted line) and calculated swivel angle(solid line) for type two task. Each row shows the comparison result for type two(LR:PP), (LR:WB), (BF:PP) and (BF:WB). The first and second columns are from subject 1 and 2, respectively.

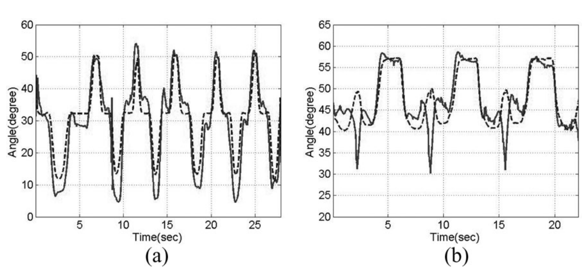

Fig. 9. Comparison between estimated swivel angle(dotted line) and calculated swivel angle(solid line) for type three task. The first and second columns are from subject 1 and 2, respectively.

3) imperfect sensor locations with respect to the anatomical body structures and the associated flexibility of the skin. Specifically in type two protocol, BF:PP and BF:WB showed similar error levels in Table I. It implies that hand orientation caused by the different types of object did not affect the estimation result. On the other hand, in the LR task, relatively high errors were observed in LR:PP. Considering the fact that LR:WB task more restricts the wrist orientation than LR:PP task does, we concluded that the torsional movement was not properly controlled in type 2 LR:PP task.

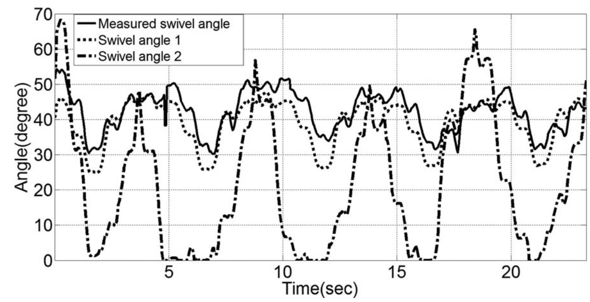

Fig. 10. Swivel angle comparison from a single subject for type one(A). The solid, dotted(Swivel angle 1) and dash-dot(Swivel angle 2) line indicate the measured swivel angle, the swivel angle based on the proposed criterion and the swivel angle based on the dynamic criterion [11]

B. Comparison With Other Constraint

To demonstrate the superiority over the other approaches, a direct comparison result with other criterion is presented in Fig. 10. Since we proposed the new redundancy resolution criterion in the kinematic level, the dynamic level criterion in [11] was selected for the comparison of estimation result. In this paper, the redundancy of the human arm movement based on the 7-DOF arm model was resolved by minimizing the magnitude of total work done by joint torques for each time step. This dynamic criteria had generated satisfactory prediction of the joint space trajectory for the fundamental motions of the human arm, such as the shoulder adduction/abduction, flexion/extension, internal/external rotation and the elbow flexion/extension.

The result in Fig. 10 shows the comparison result for a single subject who performed the type one A task. It shows that the proposed swivel angle estimation algorithm shows a better estimation performance. This might come from the fact that in our experimental condition, the speed and acceleration of each joint is restricted and low in most time duration. Let $\ddot{Q} = [\ddot{q_1}, \ddot{q_2}, \ddot{q_3}, \ddot{q_4}]$ and $\dot{Q} = [\dot{q_1}, \dot{q_2}, \dot{q_3}, \dot{q_4}]$, where q_i represents the joint angle for the ith DOF. Then, the basic dynamic equation of the human arm can be defined as $T = M\ddot{Q} + C\left(Q, \dot{Q}\right)\dot{Q} + G\left(Q\right)$ where M, $C\left(Q, \dot{Q}\right)$ and $G\left(Q\right)$ represent the matrix of moment of inertia, the centrifugal/coriolis forces and the gravity force, respectively. When the speed and acceleration of each joint get close to zero, the basic dynamic equation of the human arm can be approximated as $T \approx G\left(Q\right)$. In this case, the gravitational force becomes dominant and the swivel angle minimizing the magnitude of total work results in the elbow placed at it's lowest position, which does not explain the specific arm configuration in a static posture.

C. Application on the EXO-UL7

As a proof of concept the swivel angle estimation algorithm was incorporated with the admittance control for the upper limb exoskeleton EXO-UL7 [27]. A single subject performed a task involving the inversion of a peg-in-hole while wearing the exoskeleton. For each repetition, the swivel angle estimation was

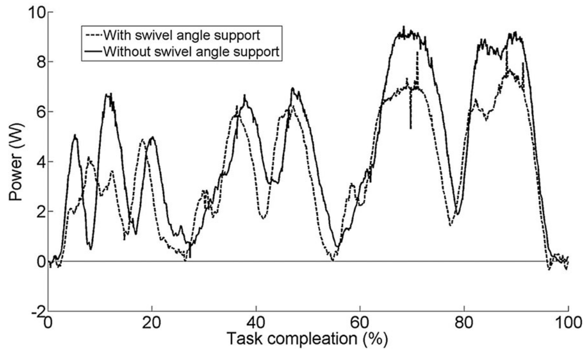

Fig. 11. Energy exchange plot between EXO-UL7 and one subject as a proof of concept test

randomly turned ON or OFF and the energy exchange between the subject and the the device was measured to assess controller performance. Fig. 11 shows the averaged energy exchange between the device and the user for both conditions. When the swivel prediction was added to the admittance control there was a 20% decrease in an energy interaction.

VI. Conclusion and Discussion

The goal of this study was to propose a criterion for resolving the human arm redundancy, verify and validate it experimentally and test it in a wearable robotic application. The proposed criterion is based on the idea that the head encapsulates a cluster of sensors and includes the input to the digestive system which is critical to sustain the life of any organism. As such the head serves as a target in a large number of unconstrained arm movements (e.g., arm reach in an unconstrained environment). It was hypothesized that the hidden mechanism of human arm reaching task is to bring an object grasped by the hand toward the head. The swivel angle was defined as an expression of the human arm redundancy. The criteria for the redundancy resolution stated that at any point in time and arm configuration during a reaching task in an unconstrained environment, the projection of the largest manipulability vector onto the virtual trajectory connecting the wrist with the head region is maximized. The experimental results indicated that the difference between the estimated swivel angle based on the proposed criteria and the swivel angle adapted by the subjects during the experiments is less than 5° on average. The experimental results also indicated that even in cases in which an object is grasped by the hand in a way that orienting this object is done within the range of motion of the wrist joint, the shoulder and elbow joint angle is not affected and the proposed criteria provides a good estimation for the swivel angle. Previous studies indicated that once the wrist joint has reach its maximal range of motion (e.g., full flexion imposed by a neurological disability such as Stroke) the shoulder and elbow joint will be affected [3].

The proposed criteria for the human arm redundancy resolution along with the kinematics equations of the arm provides a closed form mathematical solution for the human arm inverse kinematics. As such it is suitable to be incorporated into a real-time control algorithm of a 7-DOF upper limb wearable robotic system (exoskeleton). Experimental results indicated that the power used to control a wearable robotic system using an admittance control was reduced by 20% while using the proposed criterion compared to the same algorithm without it. In addition, the proposed algorithm does not require the iterative operations and complex matrix inversion commonly required in many optimization algorithms. As a result, the computational requirements are low and the solution is numerically stable that makes it suitable to be incorporated into a real-time control algorithm of an exoskeleton wearable robot, humanoid robot, or 3-D computer graphic model. Additional applications of the proposed criterion for redundancy resolution out of the scope presented in this study may be in computer animation of the human arm movements.

References

[1] J. C. Perry, J. Rosen, and S. Burns, "Upper-limb powered exoskeleton design," *Mechatronics*, vol. 12, no. 4, pp. 408–417, 2007.

[2] H. I. Krebs, M. Ferraro, S. P. Buerger, M. J. Newbery, A. Makiyama, M. Sandmann, D. Lynch, B. T. Volpe, and N. Hogan, "Rehabilitation robotics: Pilot trial of a spatial extension for mit-manus," *J. NeuroEng. Rehabil.*, vol. 1, Oct. 2004, pp. 1–15.

[3] P. Joel, J. Powell, and J. Rosen, "Isotropy of an upper limb exoskeleton and the kinematics and dynamics of the human arm," *J. Appl. Bionics Biomech.*, vol. 6, no. 2, pp. 175–191, 2009.

[4] N. I. Badler and D. Tolani, "Real-time inverse kinematics of the human arm," *IEEE Trans. Syst. Man, Cybern.*, vol. 5, no. 4, pp. 393–401, 1996.

[5] T. Asfour and R. Dillmann, "Human-like motion of a humanoid robot arm based on a closed-form solution of the inverse kinematics problem," in *Proc. IEEE/RSJ Int. Conf. Intell. Robots Syst.*, Oct. 2003, vol. 2, pp. 27–31.

[6] J. Rosen and J. C. Perry, "Upper limb powered exoskeleton," *Int. J. Humanoid Robot.*, vol. 4, no. 3, pp. 529–548, 2007.

[7] H. Kim, L. M. Miller, and J. Rosen, "Redundancy resolution of a human arm for controlling a seven DOF wearable robotic system," in *Proc. IEEE Eng. Med. Biol. Soc.*, Boston, MA, Aug. 2011, pp. 3471–3474.

[8] C. Gielen, E. J. Vrijenhoek, T. Flash, and S. Neggers., "Review of models for the generation of multi-joint movements in 3-D," *Adv. Exp. Med. Biol., Prog. Motor Control*, vol. 629, pp. 523–550, 2009.

[9] P. K. Artemiadis, P. T. Katsiaris, and K. J. Kyriakopoulos, "A biomimetic approach to inverse kinematics for a redundant robot arm," *Autonomous Robots*, vol. 29, no. 3–4, pp. 293–308, 2010.

[10] J. Soechting, C. Buneo, U. Herrmann, and M. Flanders, "Moving effortlessly in three dimensions: Does donders' law apply to arm movement?," *J. Neurosci.*, vol. 15, pp. 6271–6280, 1995.

[11] T. Kang, J. He, and S. I. H. Tillery, "Determining natural arm configuration along a reaching trajectory," *Exp. Brain Res.*, vol. 167, no. 3, pp. 352–361, 2005.

[12] Y. Uno, M. Kawato, and R. Suzuki, "Formation and control of optimal trajectory in human multi joint arm movement," *Biological Cybern.*, vol. 61, no. 2, pp. 89–101, 1989.

[13] P. Lee, S. Wei, J. Zhao, and N. I. Badler, "Strength guided motion," *Comput. Graph.*, vol. 24, no. 4, pp. 253–262, 1990.

[14] M. A.Admiraal, M. J. Kusters and S. C. Gielen, "Modeling kinematics and dynamics of human arm movements," *Motor Control*, vol. 8, no. 3, pp. 312–338, 2004.

[15] J. U. Korein, *A Geometric Investigation of Reach*. Cambridge, MA: MIT Press, 1985.

[16] N. I. Badler and D. Tolani, "Real-time inverse kinematics of the human arm," *Presence*, vol. 5, no. 4, pp. 393–401, 1996.

[17] D. Tolani, A. Goswami, and N. I. Badler, "Real-time inverse kinematics techniques for anthropomorphic limbs," *Graph. Models Image Process.*, vol. 62, no. 5, pp. 353–388, Sep. 2000.

[18] R. M. Murray, Z. Li, and S. S. Sastry, *A Mathematical Introduction to Robotic Manipulation*. Boca Raton, FL: CRC Press, 1994.

[19] L. M. Miller, H. Kim, and J. Rosen, "Redundancy and joint limits of a seven degree of freedom upper limb exoskeleton," in *Proc. IEEE Eng. Med. Biol. Soc.*, Boston, MA, Aug. 2011, pp. 8154–8157.

[20] T. Yoshikawa, *Foundations of Robotics: Analysis and Control*. Cambridge, MA: MIT Press, 1990.

[21] A. Liegeois, "Automatic supervisory control of the configuration and behavior of multibody mechanisms," *IEEE Trans. Syst. Man, Cybern.*, vol. 7, no. 12, pp. 868–871, Dec. 1977.

[22] M. S. Graziano, C. S. Taylor, and T. Moore, "Complex movements evoked by micro stimulation of precentral cortex," *Neuron*, vol. 34, no. 5, pp. 841–851, 2002.

[23] R. P. Dum and P. L. Strick, *Motor Areas in the frontal Lobe: The Anatomical Substrate for the Central Control of Movement, Motor Cortex in Voluntary Movements*. Boca Raton, FL: CRC Press, 2005.
[24] I. Stepniewska, P. C. Fang, and J. H. Kaas, “Microstimulation reveals specialized subregions for different complex movements in posterior parietal cortex of prosimian galagos,” in *Proc. Nat. Acad. Sci.*, 2012, USA, 2005, vol. 102, pp. 4878–4883.
[25] D. C. Lay, *Linear Algebra and Its Applications*, 3rd ed.: Addison Wesley, 2005.
[26] A. A. Maciejewski, “Dealing wit the ill-conditioned equations of motion for articulated figures,” *IEEE Comput. Graph. Appl.*, vol. 10, no. 3, pp. 63–71, May 1990.
[27] L. M. Miller and J. Rosen, “Comparison of multi-sensor admittance control in joint space and task space for a seven degree of freedom upper limb exoskeleton,” in *Proc. IEEE RAS EMBS Int. Conf. Biomed. Robot. Biomechatronics*, 2010, pp. 70–75.

Hyunchul Kim received the B.S. and M.S. degrees in electronic engineering both from Sogang University, Seoul, Korea, and the Ph.D. degree in electrical engineering from the University of California Santa Cruz (UCSC), Santa Cruz, in 2003, 2005, and 2012, respectively.

From 2005 to 2007, he developed wireless demodulator for DVB-H and TDMB at DTV (Digital TV) lab, LG electronics as a Research Engineer. In 2010 and 2011, he developed stroke rehabilitation system platform based on wearable robot, Exo-UL7. His research interests include the advanced control scheme for the upper limb exoskeleton robots, human–robot interaction, computer vision, statistical signal processing, and machine learning. He is now a Research Engineer in the Atromax, Inc., Santa Clara, CA, and Research Consultant in the Optodynamics, Inc., Seongnam, Korea.

Levi Makaio Miller received the B.S. degree in manufacturing engineering technology at Western Washington University, Bellingham, in 2004, the M.S. degree in mechanical engineering at the University of Washington, Seattle, in 2006, where he is currently working toward the Ph.D. degree in mechanical engineering studying powered upper limb exoskeletons for rehabilitation.

From 2008 to 2011, he was a Research Engineer at the University of California Santa Cruz and is now a Robotics Specialist at the independent consulting firm Carbon Design Group, Seattle, WA. His research interests include the human machine interface, human centered robotics, control algorithms, haptics, and neural interfaces.

Nancy Byl received the B.S. degree from the University of California San Francisco (UCSF), San Francisco, and the M.P.H. and Ph.D. degrees from the University of California, Berkeley, in 1963, 1968, and 1985, respectively.

She is a Catherine Worthingham Fellow in the American Physical Therapy Association. For ten years she was a Physical Therapist and served as the Director of physical and occupational therapy at Children’s Hospital of the East Bay and Pacific Medical Center, San Francisco. She served as a Professor and the Chair in the Department of Physical Therapy and Rehabilitation Science, School of Medicine, UCSF, developing both a masters and a doctoral program in physical therapy and an advanced doctoral degree in Rehabilitation Science. She worked in the Keck Center for Neuroscience with M. Merzenich, Ph.D., to develope a new model of aberrant learning to understand the etiology and guide intervention for focal hand dystonia. She is currently a Professor Emeritus at UCSF who collaborates with engineers to carry out translational clinical studies to quantify differences in outcomes following technology assisted rehabilitation compared to usual rehabilitative care. Her research interest includes integrating the principles of neuroplasticity to maximize function in patients with dystonia, balance disorders, stroke, and Parkinson’s Disease. She has been involved in both basic animal as well as clinical and translational research. She developed the UCSF PT Health and Wellness Center to provide an innovative site to see patients with chronic health problems and integrate new technology into practice.

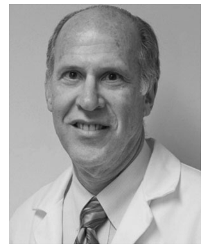

Gary M. Abrams received the Medical degree from the University of Pittsburgh, Pittsburgh, PA, in 1974, and completed a fellowship in neuroendocrinology at Columbia University, New York, NY, and the National Institute for Medical Research, Mill Hill, U.K.

He is a Professor of clinical neurology at the University of California San Francisco (UCSF), San Francisco, and the Rehabilitation Section Chief at the San Francisco VA Medical Center, San Francisco. He is an Attending Neurologist and the Director of neurorehabilitation at UCSF. He served as the Medical Director and Chief of Columbia-Presbyterian Medical Services at Helen Hayes Rehabilitation Hospital from 1986 to 1993. In 1995, he joined UCSF as an Attending Neurologist at UCSF Medical Center and the Medical Director of Rehabilitation at UCSF/Mt. Zion Medical Center, where he later served as the Chief of Neurology. His clinical and research interests include interventions for improving function after stroke and TBI. He is investigating novel methods of cognitive rehabilitation after TBI that combine behavioral and imaging outcomes. He is also evaluating new technologies for stroke treatment, including robotics and functional electrical stimulation-based orthotics. He has served as an invited consultant for the Cardiovascular, Orthopaedic, and Rehabilitation Device Panels at the FDA, as well as to industry on issues related to chronic neurological conditions.

Dr. Abrams received a Teacher-Investigator Development Award from the NIH and was a member of the neurology faculty of Columbia University from 1981 to 1995. He is currently on the Board of Directors of the American Society of Neurorehabilitation and was recently appointed to the VA Rehabilitation Research and Development Service Scientific Merit Review Board for Traumatic Brain Injury and Stroke. He is the Fellow of the American Academy of Neurology.

Jacob Rosen received the B.Sc. degree in mechanical engineering, and the M.Sc. and Ph.D. degrees in biomedical engineering from the Tel-Aviv University, Tel Aviv, Israel, in 1987, 1993 and 1997, respectively.

He is an Associate Professor in the Department of Computer Engineering, University of California Santa Cruz (UCSC), Santa Cruz. From 1987 to 1992, he served as an Officer in the IDF studying human–machine interfaces. From 1993 to 1997 he was a Research Associate developing and studying the EMG-based powered Exoskeleton at the Biomechanics Laboratory, Department of Biomedical Engineering, Tel-Aviv University. During the same period of time he held a position in a startup company developing innovative orthopedic spine/pelvis implants. From 1997 to 2000, he was a Postdoctoral Resercher in the Departments of Electrical Engineering and Surgery, University of Washington, while developing surgical robotic and medical simulation systems. From 2001to 2008, he served as a Faculty Member in the Department of Electrical Engineering, University of Washington, Seattle, with adjunct appointments with the Departments of Surgery, and Mechanical Engineering. Since 2008, he has been the Director of the Bionics Laboratory in University of California Santa Cruz (UCSC), Santa Cruz. His research interests include medical robotics, biorobotics, human centered robotics, surgical robotics, wearable robotics, rehabilitation robotics, neural control, and human–machine interface. He developed several key systems in the field of medical robotics such as the Blue and the Red Dragon for minimally invasive surgical skill evaluation that is commercialized by Simulab as the “Edge”, Raven—a surgical robotic system for telesurgery, several generations of upper and lower limb exoskeletons and most recently the Exo-UL7—a two wearable robotic systems.